ADVANCED ENERGY MATERIALS
www.advenergymat.de

Enhancing Cycle Life in Superoxide-Based Na–O_2 Batteries by Reducing Interface Reactivity

Adel Azaribeni, Alireza Kondori, Nannan Shan, Moon Gyu Park, Ahmad M. Harzandi, Ga-Yoon Kim, Mahmoud Tamadoni Saray, Arashdeep S. Thind, Pablo Navarro Munoz Delgado, Musawenkosi Ncube, Robert F. Klie, Reza Shahbazian-Yassar, Ahn T. Ngo, Larry A. Curtiss, and Mohammad Asadi**

Sodium–oxygen (Na–O_2) batteries are considered a promising energy storage alternative to current state-of-the-art technologies owing to their high theoretical energy density, along with the natural abundance and low price of Na metal. The chemistry of these batteries depends on sodium superoxide (NaO_2) or peroxide (Na_2O_2) being formed/decomposed. Most Na–O_2 batteries form NaO_2, but reversibility is usually quite limited due to side reactions at interfaces. By using new materials, including a highly active catalyst based on vanadium phosphide (VP) nanoparticles, an ether/ionic liquid-based electrolyte, and an effective sodium bromide (NaBr) anode protection layer, the sources of interface reactivity can be reduced to achieve a Na–O_2 battery cell that is rechargeable for 1070 cycles with a high energy efficiency of more than 83%. Density functional theory calculations, along with experimental characterization confirm the three factors leading to the long cycle life, including the effectiveness of the NaBr protective layer on the anode, a tetraglyme/EMIM-BF_4 based electrolyte that prevents oxidation of the VP cathode catalyst surface, and the EMIM-BF_4 ionic liquid aiding in avoiding electrolyte decomposition on NaO_2.

1. Introduction

Non-aqueous sodium–oxygen (Na–O_2) batteries are considered a promising energy storage alternative for currently available lithium-based batteries owing to their high gravimetric energy density, and more specifically, the natural abundance and low price of Na metal that can lead to an inexpensive and low-weight battery technology.[1–6] The chemistry of sodium–oxygen batteries is controlled by two possible discharge products: sodium superoxide (NaO_2) and sodium peroxide (Na_2O_2). As they both have very close Gibbs free energies of formation (−437.5 and 459 kJ mol^{-1}, respectively), both will be thermodynamically feasible products during the discharge process.[7–9,10]

The formation mechanisms and kinetics of NaO_2 and Na_2O_2 can differ significantly. In Na–O_2 cells, the oxygen

A. Azaribeni, A. Kondori, A. M. Harzandi, G.-Y. Kim, P. N. M. Delgado, M. Asadi
Department of Chemical and Biological Engineering
Illinois Institute of Technology
Chicago, IL 60616, USA
E-mail: m.asadi@iit.edu

N. Shan, M. G. Park, A. T. Ngo, L. A. Curtiss
Materials Science Division
Argonne National Laboratory
Lemont, IL 60439, USA
E-mail: curtiss@anl.gov

N. Shan, M. Ncube, A. T. Ngo
Department of Chemical Engineering
University of Illinois – Chicago
Chicago, IL 60607, USA

M. T. Saray, R. Shahbazian-Yassar
Department of Mechanical and Industrial Engineering
University of Illinois – Chicago
Chicago, IL 60607, USA

A. S. Thind, R. F. Klie
Department of Physics
University of Illinois – Chicago
Chicago, IL 60607, USA

The ORCID identification number(s) for the author(s) of this article can be found under https://doi.org/10.1002/aenm.202404703

DOI: 10.1002/aenm.202404703

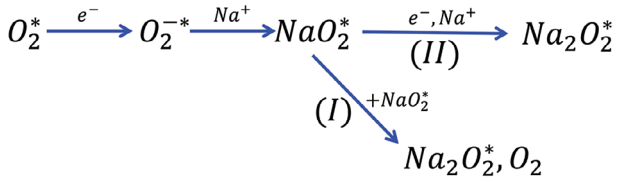

Figure 1. The schematic mechanism in the formation of NaO_2 and Na_2O_2 in the Na–O_2 cell batteries.

(O_2) is reduced to superoxide anion (O_2^-) at cathode surface through a catalytic process. This one-electron reaction is relatively simple and fast. The Na^+ ions then react with O_2– to form NaO_2 (**Figure 1**). The growth of NaO_2 can occur via two mechanisms, 1) solution-based or 2) surface-based. In the surface-based mechanism, NaO_2 grows directly on the cathode surface;[11,12] while, in the solution-based mechanism, NaO_2 desorbs into the electrolyte solution. As its concentration increases and reaches supersaturation, it precipitates on the cathode surface.[12,13] The formation of Na_2O_2 can also occur in several possible ways. The NaO_2 can undergo chemical disproportionation to form Na_2O_2(Figure 1, pathway I) either on the surface or in solution and release O_2.[14–16] The Na_2O_2 can also form via adding a second electron to NaO_2 in a surface reaction (Figure 1, pathway II). A number of factors can affect the kinetics of these processes. As discussed later, NaO_2 disproportionation to Na_2O_2 (I) has a significant energy barrier, which makes this pathway less likely. The formation of Na_2O_2 via addition of a second electron and Na^+ ion (II in Figure 1) will depend on various factors such as kinetics of reduction of NaO_2 on the surface, as well as cell configuration that is not well understood.[14]

Numerous studies have confirmed the formation of NaO_2 as the main discharge product in Na–O_2 battery cells in a single electron reaction in commonly used electrolytes (ether-based), potentially offering a battery with high energy density.[4,5,17,15,18–20] However, cyclability and long-term stability of Na–O_2 batteries based on NaO_2 remain as major challenges due to reactivity at the surfaces of the cathode, anode, and discharge product, resulting in irreversible formation and decomposition of NaO_2.[21,22]

Recently, nitrogen-doped carbon nanofibers and 0.5 M sodium triflate in tetraethylene glycol dimethyl ether (tetraglyme or TEGDME) were used in a Na–O_2 battery cell.[23] The results indicated a reversible formation/decomposition of a film-like NaO_2 layer at a current density of 200 mA g^{-1} and capacity of 500 mAh g^{-1} for 90 cycles. In another study, vertically aligned carbon nanotubes and 0.5 M sodium triflate in tetraglyme were shown to reversibly form and decompose nanosized NaO_2 particles for 100 cycles at a low current density of 67 mA g^{-1} and a capacity of 750 mAh g^{-1}.[24] While these results and others[25–27] indicate some improvements, the limited cycle life, low current rates, and low capacities hamper the realization of Na–O_2 battery technology. These are mainly attributed to i) the lack of a highly active and stable catalyst to form and decompose NaO_2 at high rates and low overpotentials, ii) reactions of electrolytes with the NaO_2 discharge product, and iii) the high reactivity of the Na anode with the electrolyte, sodium salts, and O_2, resulting in both the consumption of the electrolyte and the excessive corrosion of the Na anode.[6,21,25–28]

Here, we report a Na–O_2 battery cell composed of vanadium phosphide (VP) nanoparticles at the cathode that works in synergy with an aprotic tetraglyme/ionic-liquid electrolyte to reduce sources of interfacial reactivity and reversibly form/decompose NaO_2 nanoparticles via a solution-mediated pathway as the sole discharge product, with a NaBr protection layer on anode surface, for 1070 cycles at a capacity of 1000 mAh g^{-1} and with a high energy efficiency of more than 83%. The protection layer is needed to prevent parasitic reactions and enable the long cycle life. Our results indicate that the Na–O_2 battery cell has a low polarization gap of ≈100 mV at the first cycle. Different electrochemical and physicochemical characterization techniques, that is, Raman spectroscopy, X-ray diffraction (XRD), X-ray photoelectron spectroscopy (XPS), differential electrochemical mass spectroscopy (DEMS), and scanning electron microscopy (SEM) are used to understand the chemistry of the cell, the role of VP nanoparticles, and the stability of cell components. Density functional theory (DFT) is used to investigate the Na anode protection, the role of the ionic liquid, and the formation of NaO_2.

2. Results and Discussion

We initially investigated the performance of five transition metal phosphide (TMP) nanoparticles, that is, VP, molybdenum phosphide (MoP), tri-molybdenum phosphide (Mo_3P), di-iron phosphide (Fe_2P), tri-iron phosphide (Fe_3P), and di-nickel phosphide (Ni_2P). They were synthesized using a chemical vapor transport (CVT) method followed by mechanical ball-milling (Section S1.1, Supporting Information). All were characterized by XRD and XPS. The XRD pattern of the VP nanoparticles chosen for this study is shown in **Figure 2a**, where peaks at 28.7°, 32.5°, 35.7°, and 44.0° 2θ degrees correspond to (002), (100), (101), and (102) facets, respectively, confirming the crystalline structure of the synthesized nanoparticles with an average crystallite size of ≈56 nm (Section S2, Supporting Information). Figure 2b,c shows high-magnification high-angle annular dark field (HAADF) scanning transmission electron microscopy (STEM) images of a VP particle (from a region shown in Figure S2a in Section S3, Supporting Information), with the corresponding fast Fourier transform (FFT) pattern of Figure 2c along [111] axis. The magnified inverse FFT (IFFT), along with a superimposed VP atomic model at [111] zone axis (Figure 2d) confirms the hexagonal crystal structure of the VP nanoparticles. More STEM analysis of the VP nanoparticles is explained in Section S3, Supporting Information. The XRD characterization of the other nanoparticles is given in Section S1.1, Supporting Information.

Figure 2e,f shows the V 2*p* and P 2*p* XPS spectra of the VP nanoparticles, respectively (Section S4, Supporting Information). Peaks at binding energies of 512.4 and 520 eV (Figure 2e) indicate the standard V $2p_{3/2}$ and V $2p_{1/2}$ peaks of V^0. Compared to metallic vanadium (511.7 and 519.3 eV), the binding energies of the V $2p_{3/2}$ and V $2p_{1/2}$ in VP are up-shifted by ≈0.7 eV, which indicates the formation of V—P bonds. Moreover, the P 2*p* spectrum of VP shows the doublet peaks at 128 and 128.9 eV (P $2p_{3/2}$ and P $2p_{1/2}$, respectively) that are negatively shifted compared with that of elemental phosphorus, in agreement with the formation of VP structure. Details of the XPS characterization of the other TMPs are given in Section S1.1, Supporting Information.

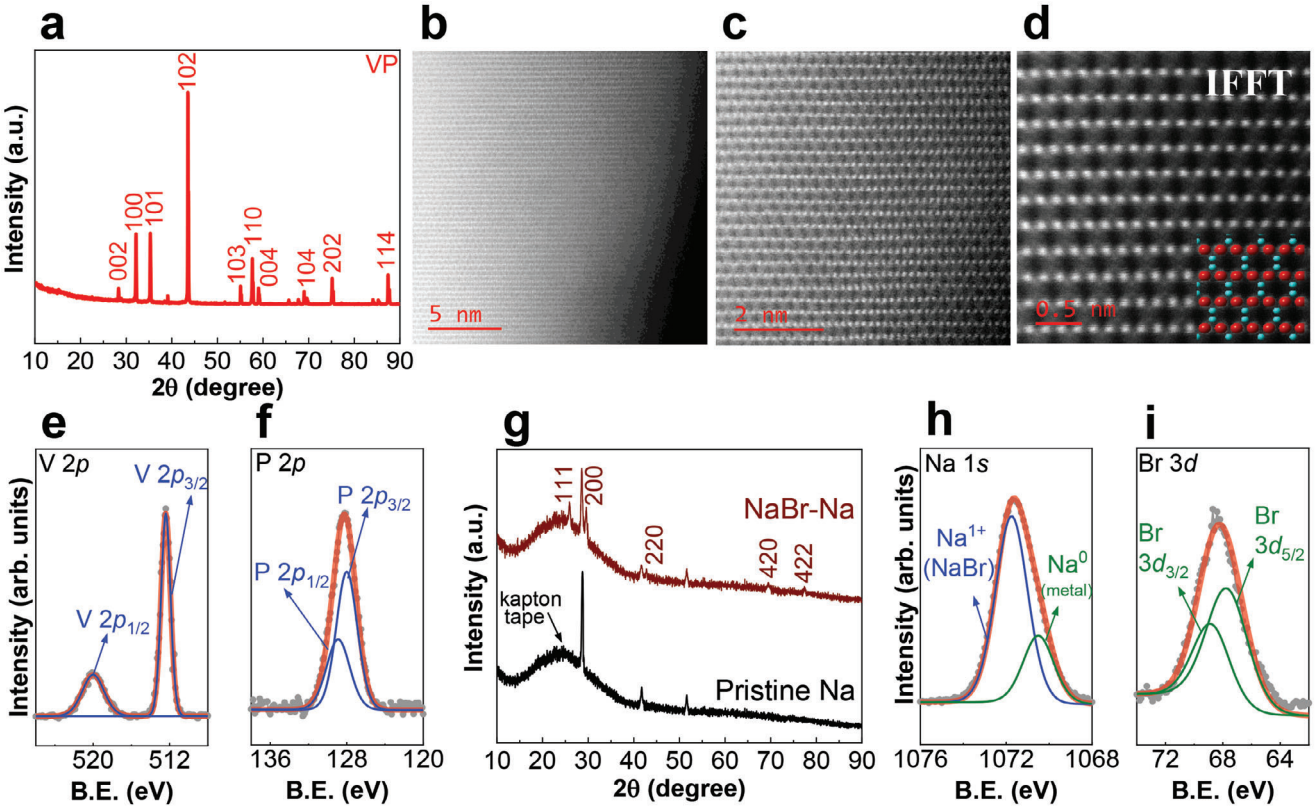

Figure 2. Characterization of the VP nanoparticles as the cathode and the NaBr protection layer for the Na anode used in the Na–O_2 battery cell. a) Diffraction pattern of the VP nanoparticles and b,c) high magnification HAADF-STEM images of the VP nanoparticles. Inset in Figure 2c shows the fast Fourier transform (FFT) pattern of image (c) along [111] zone axis. d) Magnified inverse FFT (IFFT) along with superimposed VP atomic model at [111] zone axis, with red and cyan spheres representing V and P atomic columns. e,f) V 2*p* and P 2*p* XPS spectra of the VP nanoparticles and g) diffraction pattern of the NaBr protected Na anode compared to that of pristine Na anode. h,i) Na 1*s* and Br 3*d* XPS spectra of the NaBr protected Na anode. Characterization of other TMPs is explained in Section S1, Supporting Information.

We evaluated the electrochemical performance of the TMP nanoparticles, that is, VP, MoP, Mo_3P, Fe_2P, Fe_3P, and Ni_2P as the cathode catalyst in a two-electrode system (Section S5.2, Supporting Information). The cyclic voltammetry (CV) results indicated VP nanoparticles have higher current density and lower overpotential for both ORR and OER, suggesting a better catalytic activity for these reactions (Figure S4 in Section S5.2, Supporting information). Moreover, we used the VP nanoparticles and other TMP nanoparticles as the cathode catalyst in a Na–O_2 battery cell under pure O_2 environment to further investigate the electrocatalytic performance of these materials. The cathode was prepared by coating a mixture of TMP nanoparticles and Vulcan XC-72R with mass ratio of 9:1 on a gas diffusion layer (GDL) with a geometrical surface area of 1 cm^2. The cathode material loading on the GDL was controlled to be 0.1 mg cm^{-2}. A 1 M sodium bis(trifluoromethylsulfonyl)imide (NaTFSI) salt dissolved in a 3:1 %v/v of tetraglyme:1-Ethyl-3-methylimidazolium tetrafluoroborate (EMIM-BF_4) mixture, with 25 mM each of 2,2,6,6-tetramethyl-1-piperidinyloxyl (TEMPO) and 2,5-di-tert-butyl-1,4-benzoquinone (DBBQ) redox mediators (RMs). The 3:1 %v/v of tetraglyme:EMIM-BF_4 mixture was utilized as the electrolyte because adding EMIM-BF_4 showed to improve the ionic conductivity of the electrolyte and catalytic performance of VP nanoparticles (Section S5.3, Supporting Information). The redox mediators could act as electron transfer agents from the cathode to reduce oxygen in the electrolyte.[29] As shown in Figure S6 in Section S5.4, Supporting Information, VP nanoparticles can operate for ≈230 continuous cycles without any Na anode protection, whereas other TMP nanoparticles, that is, MoP, Mo_3P, Ni_2P, Fe_3P, and Fe_2P show relatively smaller cycle life and higher potential gaps during the discharge and charge processes. The better performance of VP can be attributed to better OER/ORR electrocatalytic activities. Therefore, VP nanoparticles were selected to be the cathode catalyst in a Na–O_2 battery cell under a pure O_2 environment.

To improve the performance of the developed Na–O_2 battery, we also utilized a NaBr anode protection coating combined with the VP nanoparticles as the cathode catalyst and tetraglyme:EMIM-BF_4-based electrolyte. As for the anode, a NaBr anode protection layer was chemically synthesized by drop casting of 1-bromopropane on sodium metal anodes and drying under vacuum (Section S5.5, Supporting Information). Comparing the XRD patterns of a pristine Na anode with the NaBr-protected Na anode (Figure 2g) indicates peaks at 26.0°, 29.5°, 42.8°, 69.5°, and 77.5° that could be attributed to the (111), (200), (220), (420), and (400) facets of NaBr, respectively, confirming the presence of a NaBr coating as the protection layer. We also carried out XPS experiments for the NaBr protected anode to confirm the

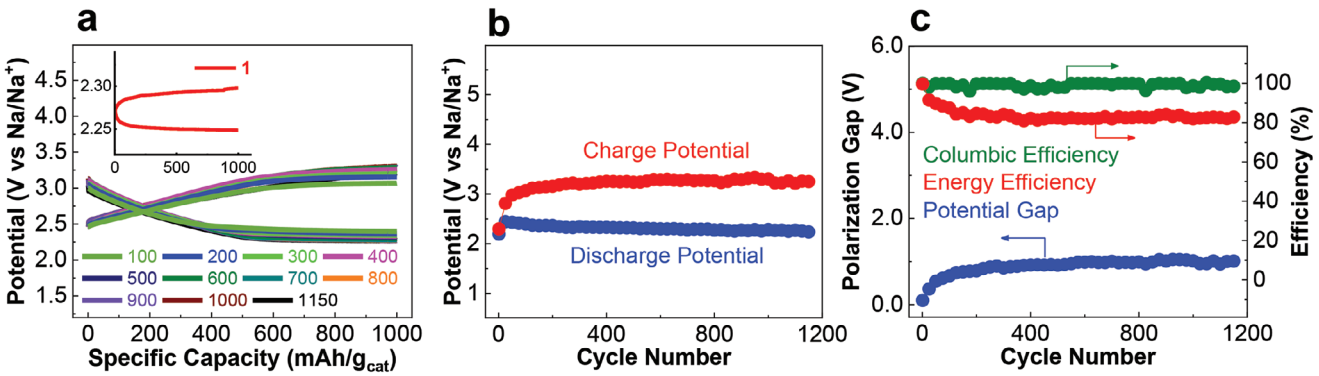

Figure 3. The Na–O_2 battery cell performance using VP cathode and NaBr protected Na anode. a) Charge/discharge profiles over 1070 cycles at a constant density of 1 A g^{-1} and a constant capacity of 1 Ah g^{-1}. The electrolyte is 1 M NaTFSI dissolved in TEGDME:EMIM-BF_4 (3/1 v/v%) with 25 mM each of TEMPO and DBBQ RMs. b) Discharge and charge potential values over 1070 cycles. c) Changes in coulombic efficiency, energy efficiency, and polarization gap over 1070 cycles.

chemical composition (Figures 2h and 2i, respectively). Our XPS results indicate peaks at 1070.5 and 1071.8 eV for Na 1s, each of which is relevant to the presence of metallic sodium (Na^0) and the Na^{1+}, with the single ion pair in the form of the NaBr. Moreover, the Br 3d spectrum of the Na anode shows Br 3d3/2 and Br 3d5/2 standard peaks at 67.8 and 68.9 eV, confirming the predominant presence of metallic—bromide bonds on the Na anode in the form of NaBr. The detailed fabrication procedure and characterization experiments for the NaBr coating as well as two others, sodium chloride (NaCl) and sodium iodide (NaI) examined in this study, are provided in Sections S5.5 and S5.6, Supporting Information.

The battery cycling experiments shown in **Figure 3a** were performed at room temperature under constant discharge and charge current densities of 1 A g^{-1} (0.1 mA cm^{-2}) and a capacity of 1 Ah g^{-1} measured based on the total mass of the cathode materials, that is, VP nanoparticles and Vulcan XC-72R (0.1 mg cm^{-2}) after 24 h rest time under the pure O_2 environment. Figure 3a displays the discharge and charge profiles of the Na–O_2 battery cell over 1070 continuous discharge–charge cycles. As shown in the inset of Figure 3a, the cell potential decreases to 2.25 V versus Na/Na^+ after 1 h of discharge process at the 1st cycle (Section S5.6, Supporting Information). Over the following charge process, the cell potential increases to 2.30 V versus Na/Na^+, yielding a polarization gap of only 50 mV at the capacity of 1 Ah g^{-1} at the 1st cycle. Figure 3b shows discharge and charge potential variation over 1070 cycles. As shown in this figure, we observe a fairly constant discharge potential over the 1070 cycles (≈2.25 V vs Na/Na^+). However, the charge potential increases from 2.3 (first cycle) to 3.20 V (last cycle) versus Na/Na^+ over the course of cycling up to cycle 1070.

The variations in coulombic efficiency (C.E.), energy efficiency, and polarization gap of the Na—O_2 battery cell at a current density of 0.1 mA cm^{-2} are shown in Figure 3c. As illustrated in the figure, the Na–O_2 battery cell demonstrates a coulombic efficiency of 100% over 1070 cycles of galvanostatic cycling at a current density of 0.1 mA cm^{-2} (green dots in Figure 3c). The primary reason for the 100% coulombic efficiency is due to the same capacity obtained on both discharge and charge processes that can be attributed to the excess amounts of sodium and oxygen in the cell. The polarization gap (blue dots in Figure 3c) consists of two different regions, i) from cycle 1 to 150 where the polarization gap increases from 100 mV at the 1st cycle to 0.76 V at the 150th cycle and ii) from cycle 151 to cycle 1070 with a gradual increase from 0.76 to 1.07 V. Moreover, the Na–O_2 battery cell exhibits an energy efficiency of more than 83% for over 1070 cycles. In addition, the Na–O_2 cell exhibits cycling after 1070 cycles up to 1222 cycles where the cell fails (Section S5.6 and Figure S14, Supporting information). Figure S14, Supporting information indicates discharge and charge potential drops to 2 and 2.75 V, respectively, that can be attributed to potential degradation of cell components after 1070 cycles.

We also examined the rate capability of the developed Na–O_2 battery cell at different current densities (0.05, 0.1, and 0.2 mA cm^{-2}, respectively; Figure S15 and Section S5.7, Supporting Information). The results indicate that the developed Na–O_2 battery can also operate at a faster rate; however, the charging and discharge potentials differ.

We have compared the results for our Na–O_2 battery with other reported Na–O_2 batteries (Table S2 in Section S6, Supporting Information). As shown in this table, our Na–O_2 battery worked around 2140 h (1070 cycles at 0.1 mA cm^{-2}), that is 10 times more than the best performing Na–O_2 battery, which operated for ≈200 hours (400 cycles at 0.6 mA cm^{-2}).[30] Moreover, as shown in Table S2, Supporting Information, other studies reported their performance analyses with a current density between 0.01 and 0.1 mA cm^{-2} that highlights the enhanced performance of our Na–O_2 cell under a current density of 0.1 mA cm^{-2}.

The performance of Na–O_2 battery cells using NaI and NaCl protected Na anode is also shown in Figure S11 in Section S5.6, Supporting Information. Our results indicate that the Na–O_2 battery based on a NaBr anode protection coating outperforms the batteries based on the NaI and NaCl anode protection coatings under identical experimental conditions by exhibiting the highest cycle life of 1070 (vs 650 for NaI and 260 for NaCl).

To gain more insight about the reason behind the higher performance of the NaBr anode protection coating in our Na–O_2 battery cell, we performed a DFT computational study of one layer of NaCl, NaBr, or NaI on an Na surface (Section S7.1, Supporting

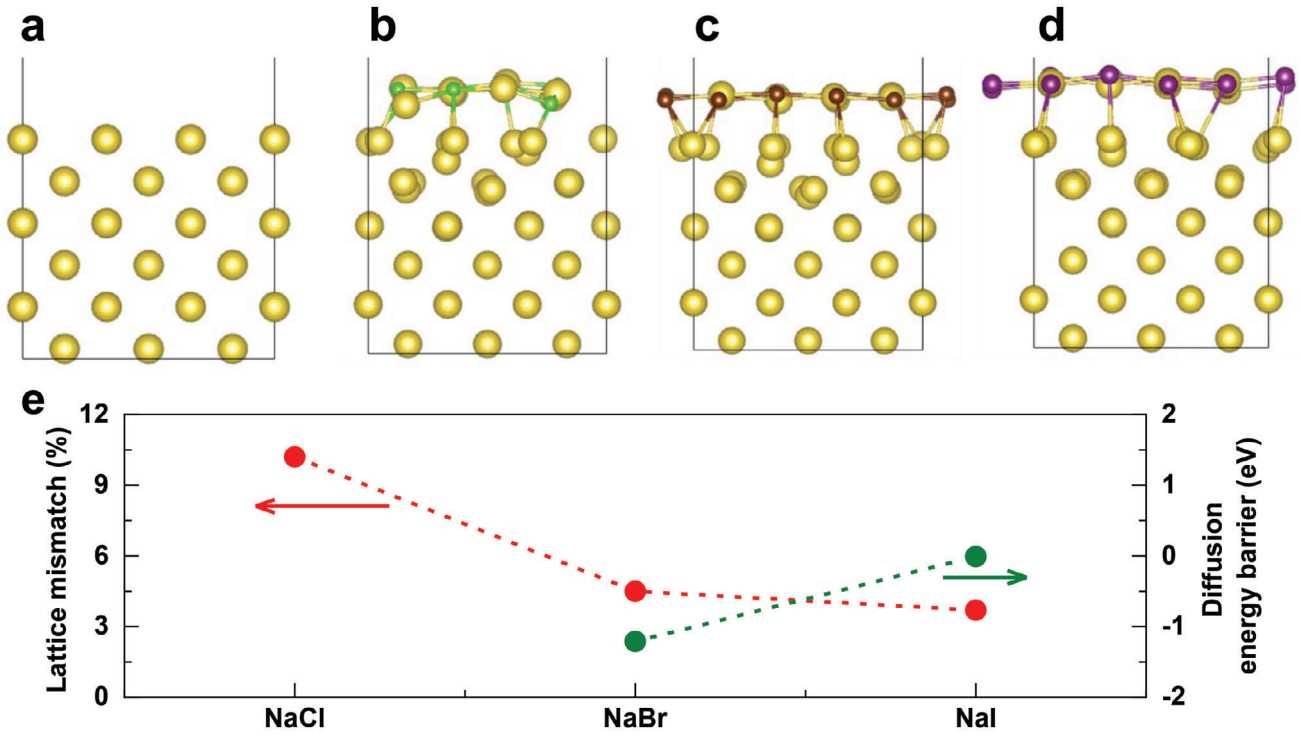

Figure 4. DFT optimized anode structures: a) Na (200) surface and the b) NaCl, c) NaBr, and d) NaI layers on the Na (200) surface. The Na, Cl, Br, and I atoms are in gold, green, brown, and purple, respectively. e) The lattice mismatch (%) and diffusion energy barrier (eV) for protection layers NaBr, NaCl, and NaI.

Information) as a model for the protection coating. Our simulation of one layer of NaCl (200), NaBr (200), and NaI (200) on bulk (three-layer) Na (200) surfaces resulted in the lattice mismatches to the Na surface of 10.2%, 4.5%, and 3.7% for NaCl, NaBr and NaI, respectively (**Figure** 4a–e).

Based on the best lattice matches for NaBr and NaI, we evaluated the diffusion of Na from different locations on the Na surface through the NaBr and NaI layers. The most negative diffusion energies were computed to be −1.21 and −0.01 eV for NaBr and NaI layers, respectively, which indicated that it is easier for Na atom diffusion to the surface with a NaBr layer than that with a NaI layer (Figure 4e). Thus, based on the lattice mismatch and Na diffusion energy calculations, the modeling suggested that a NaBr protective coating is more efficient compared to a NaI layer, and this helps to explain the experimental observations in Figure 3; Figure S11 in Section S5.6, Supporting Information. In addition, effective NaBr anode protecting layers protect the sodium anodes from pristine reaction between superoxide anions due to oxygen crossover and the decomposition of the electrolyte by sodium metal (Figure S13 in Section S5.6, Supporting Information). As shown in Figure S13, Supporting Information, the XRD result indicates no additional peak related to sodium oxides or sodium hydroxides, suggesting no reaction between electrolyte and our developed NaBr protection layer.

To characterize the chemistry of the cell and identify discharge products in our new Na–O_2 battery cell, we first performed SEM imaging experiments to determine the morphology and distribution of the discharged cathode sample (Section S8, Supporting Information). **Figure** 5a shows the SEM image of the discharged cathode sample at capacity 1.0 mAh cm^{-2}, wherein cube-like NaO_2 nanoparticles of size from 500 nm to 2 μm could be detected.

We have also conducted conductive atomic force microscopy (C-AFM) to study the morphology of the cathode after discharge and charge compared with the pristine cathode (Section S9, Supporting Information). Figure S22, Supporting Information shows the C-AFM images of a) pristine cathode, b) 10th cycle discharge, and c) 10th cycle charge. The C-AFM results indicate the conductivity of the cathode decreases after the 10th cycle (Figure S22a,b, Supporting Information). This can be attributed to the formation of the insulating discharge product (NaO_2); while, after charge, we observed the conductivity of the cathode increased (Figure S22c, Supporting Information). This indicates that the formed NaO_2 during the discharge process was decomposed after the charge process.

To identify the cathode products, we then carried out Raman spectroscopy experiments (Figure 5b) for the discharged and charged cathode samples at different cycles, that is, 1, 100, and 200, and compared them with the pristine cathode sample. Comparing the Raman spectra of the cycled cathodes with the pristine cathode indicates that peaks at 852, 950, and 1042 cm^{-1} were attributed to VP nanoparticles, whereas peaks at 1355 and 1585 cm^{-1} were relevant to those of the D and G bands of Vulcan XC-72R and the GDL (Figure S23 in Section S10, Supporting Information). However, a Raman peak at ≈1156 cm^{-1} (depicted with red asterisk) could be seen in all the discharged cathode samples, which is an indication of NaO_2 formation during the discharge processes. As shown in Figure 5b; Figure S23, Supporting

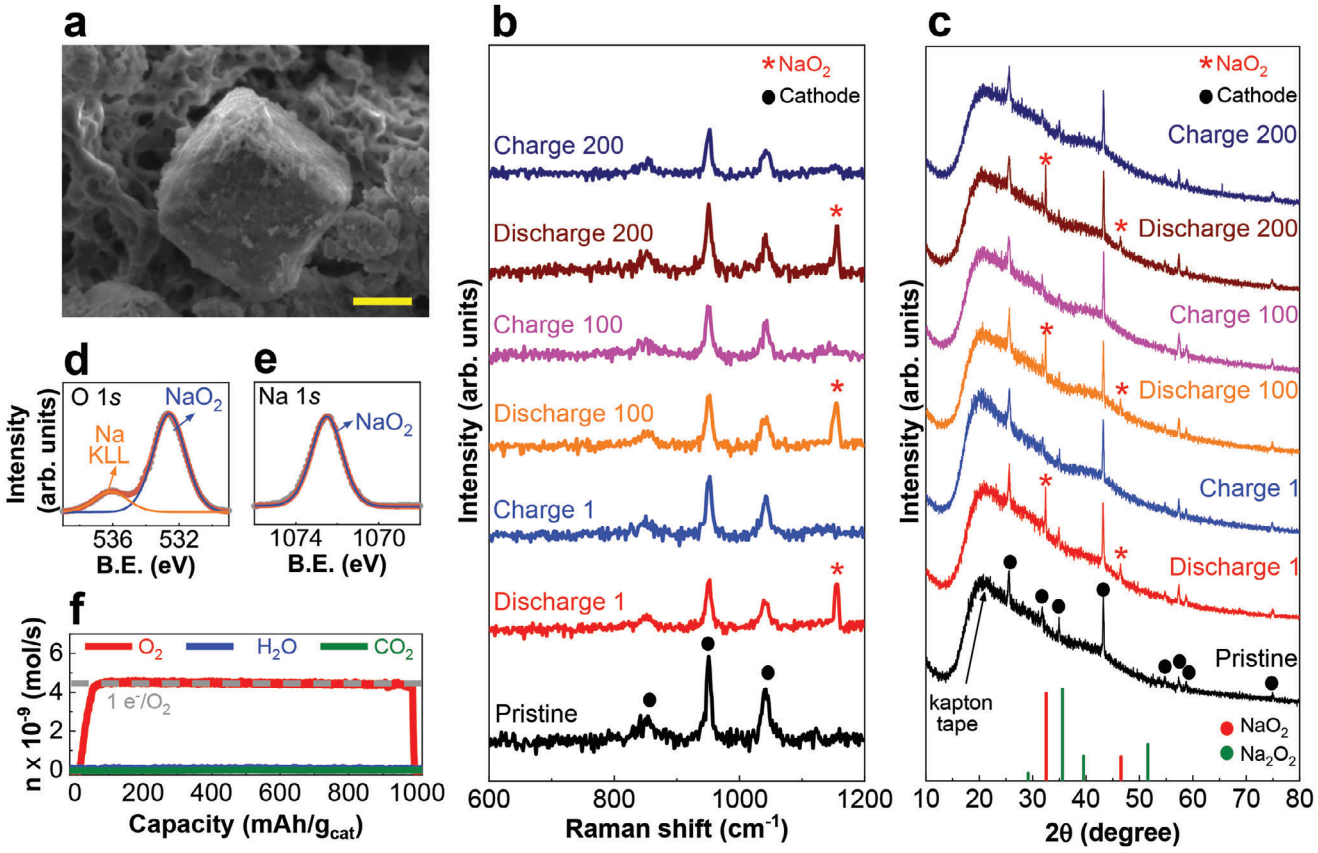

Figure 5. Characterization of the discharge and charge processes in the Na–O_2 battery cell. a) High magnification SEM image of the discharged cathode (scale bar, 1 µm). b) Raman spectra of the discharged and charged cathodes. c) Diffraction patterns of the discharged and charged cathodes. d,e) Na 1s and O 1s XPS spectra of the discharged cathodes. f) In situ DEMS experiment for the charge process.

Information, there was no such peak (1156 cm^{-1}) in the charged cathode samples, meaning that NaO_2 was reversibly decomposed in the following charge processes. We also did not find any Raman peaks relevant to those of Na_2O_2, $Na_2O_2.2H_2O$, NaOH, and Na_2CO_3 suggesting NaO_2 was the sole product of the developed Na–O_2 battery. Moreover, the standard Raman peaks marked with black circles remained unchanged in all the cycled cathode samples, which indicates the high stability of the VP nanoparticles.

To study the effect of the EMIM-BF_4 and redox mediators in the chemical composition of the discharge products, we also perform Raman spectroscopy experiments for four different electrolyte compositions of i) TEGDME electrolyte, ii) TEGDME/ionic liquid electrolyte, iii) TEGDME/ionic liquid with DBBQ, and iv) TEGDME/ionic liquid with TEMPO (Figure S24 in Section S11, Supporting Information). The results show that in the case of ionic liquid/TEGDME, NaO_2 is the sole cathode product; while, by using only TEGDME electrolyte, both Na_2O_2 and NaO_2 are produced as discharge products (Figure S25 in Section S11, Supporting Information). This is a reason for the increased potential gap in the case of using only the TEGDME electrolyte, which is also consistent with the many other studies that showed the formation of Na_2O_2 could contribute to a high polarization gap in Na–O_2 batteries.[27] Furthermore, the Raman spectroscopy results indicated that NaO_2 is the only cathode product formed by using the EMIM-BF_4 ionic liquid/TEGDME electrolyte with and without TEMPO and DBBQ (Figure S25 in Section S11, Supporting Information).

We have also studied the stability of the electrolyte by performing nuclear magnetic resonance (NMR) H-NMR and ^{13}C-NMR spectroscopy of the fresh and used electrolytes (Section S12, Supporting Information). The results show no change in the NMR spectra of the used electrolyte, indicating that the EMIM-BF_4 ionic liquid/TEGDME electrolyte is stable in the Na–O_2 cells (Figure S26, Supporting Information).

We performed XRD experiments to gain more insight into the type of the discharge product (NaO_2) and its reversibility at different cycles, that is., 1, 100, and 200 (Section S13, Supporting Information). The diffraction pattern of the discharged cathode sample at the first cycle indicated new peaks at 32.5° and 46.5° compared with the pristine cathode (Figure 5c), which were attributed to the (200) and (220) reflections of NaO_2 nanoparticles. No characteristic peak related to those of Na_2O_2, $Na_2O_2.2H_2O$, NaOH, and Na_2CO_3 was found in the diffraction patterns of the discharged cathode samples, which was also in agreement with the Raman spectroscopy experiment. Moreover, after the charge process of the first cycle, the two peaks relevant to NaO_2 disappeared completely, meaning that the NaO_2 discharge product was fully removed by oxidation in the charge process. This trend is similar in higher cycle numbers, for example, 100 and 200. It is also important to note that the peaks at 25.6°, 31.8°, 35°, 43.2°,

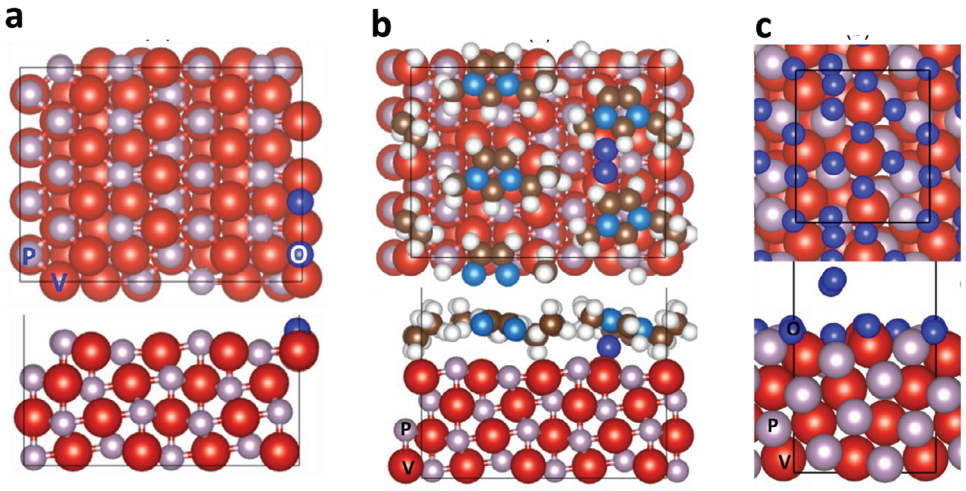

Figure 6. DFT optimized cathode surfaces with O_2 adsorption: a) VP(102), b) VP (102) covered by EMIM, and c) VP (102) covered by O. The V, P, C, N, H, and O atoms are in red, light purple, brown, light blue, white, and dark blue, respectively.

54.8°, 57.4°, 58.8°, and 75°, marked with black circles and relevant to the pristine cathode sample, remained unchanged in all cycled samples, which reflects the high stability of the cathode.

Next, a set of XPS experiments was carried out to study both the chemical composition of the discharge product formed at the cathode surface (Figure 5d,e) and the VP nanoparticles over the course of cycling (Figures S27 and S28 in Section S14, Supporting Information). Figure 5d shows the O 1*s* spectra of the discharged cathode sample at the first cycle with a peak at 532.6 eV, indicating more content of oxygen-rich phases of sodium, that is, NaO_2, and also a smaller Auger peak at 536 eV (Na KLL). A similar understanding could be obtained from the Na 1*s* spectra depicted in Figure 5e, where a peak at 1072.5 eV was correlated to the formation of NaO_2 phase according to the literature. Moreover, the V 2*p* spectra of the cycled cathode sample compared with that of a pristine cathode sample indicated the formation of oxide-phases, that is, VO and V_2O_5, suggesting partial oxidation of the VP nanoparticles over the course of cycling under an oxygen-rich environment (Figure S28 in Section S14, Supporting Information). Comparing this result with that of Raman and XRD experiments for the cycled cathode sample (Figures 5b and 5c, respectively), we concluded that the formed VO and V_2O_5 at higher cycle numbers were in small amounts as there was no indication of such oxide phase observed in the Raman spectroscopy and XRD experiments.

In order to confirm the chemical composition of the discharge product, we also carried out an in situ DEMS experiment and measured the number of electrons transferred per O_2 during the charge process (Section S15, Supporting Information). Our in situ DEMS result shown in Figure 5f indicated an immediate increase of the O_2 signal that remained constant at 4.5×10^{-9} mol s^{-1} during the charge process; while, the CO_2 and H_2O signals remained unchanged. This shows that the chemical composition of the discharge product was of an oxide species without any H_2O ($Na_2O_2.2H_2O$ and NaOH) or CO_2 (Na_2CO_3) content. Furthermore, the measured number of electrons transferred per O_2 also indicated $e^-/O_2 = 1.00$, which was attributed to the decomposition of NaO_2 via a single electron transfer reaction. This result is consistent with Raman spectroscopy, XRD, and XPS results confirming NaO_2 is the only discharge product for the developed Na–O_2 battery.

We then performed a mechanistic study to gain insight into the long cycle life in this Na–O_2 battery, by using both experimental and computational methods. At first, to provide insight about the discharge process of this Na–O_2 battery cell, we performed a DFT investigation of O_2 adsorption on a VP (102) surface (Section S7.2, Supporting Information). The (102) surface of VP was chosen for this study based on our observations from the XRD results (Figure 2a). To do so, we first studied the O_2 adsorption on VP (102) surface (**Figure 6**a). Our results indicate that the VP (102) pristine surface was extremely active and resulted in O_2 dissociation as shown in this figure. As the ionic liquid molecules could adsorb on the VP surface as well, we performed simulations with EMIM cations on a VP (102) surface with different coverages as shown in Figure S18 in Section S7.2, Supporting Information. Using the high EMIM coverage of the VP (102) surface, we introduced O_2 into the model again and found that O_2 adsorbs on a V–V bridge site in molecular form, as shown in Figure 6b; Figure S19a in Section S7.2, Supporting Information. This suggests that the ionic liquid molecules are helpful in preventing O_2 dissociation on the pristine VP (102) surface. Without the presence of the ionic liquid, it is possible that the VP surface will be partially or fully oxidized due to its high activity for O_2 dissociation. We tested O_2 adsorption on a fully oxidized VP (102) surface and found that O_2 will not bind on a fully oxidized VP (102) surface anymore as displayed in Figure 6c, consistent with the poor performance for the electrolyte without the EMIM ionic liquid.

The NaO_2 discharge product is likely formed by a through-solution nucleation and growth mechanism based on several previous studies of Na–O_2 batteries with ether-based electrolytes.[6,31,32] Lutz et al.,[33] using fast imaging transmission electron microscopy, found that NaO_2 cubes form during reduction by a solution-mediated nucleation process and that the subsequent oxidation of NaO_2 also proceeds via a solution mechanism. Sheng et al.[34] determined that in medium to high donor number electrolytes (such as diglyme and DMSO),

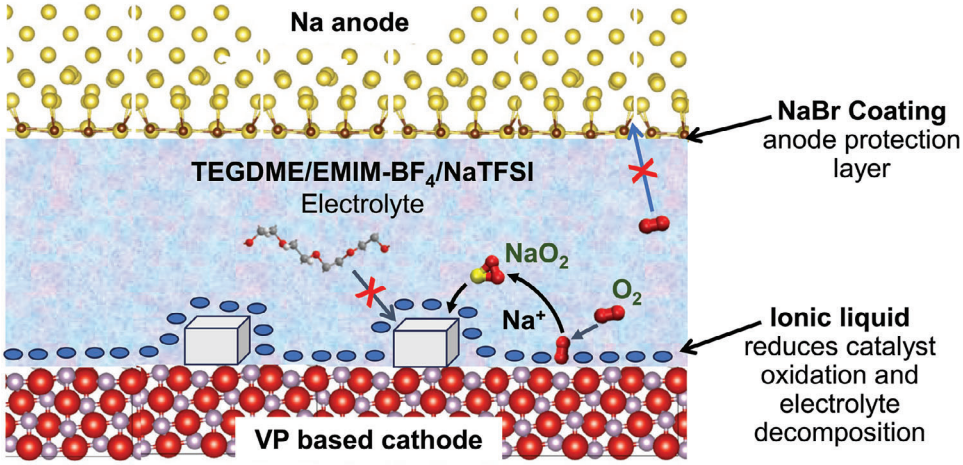

Figure 7. Schematic of the NaO_2 battery illustrating how a NaBr protective coating on the anode, a tetraglyme/EMIM-BF_4 based electrolyte, and the VP cathode catalyst act to reduce interfacial reactivity.

solution-phase formation of NaO_2 is favored over disproportionation to Na_2O_2; while, in low donor number electrolytes (such as acetonitrile), Na_2O_2 formation is favored by a surface reaction. Thus, the tetraglyme/EMIM-BF_4 based electrolyte used in this study is likely to favor solution-phase NaO_2, formation leading to nucleation and growth of the observed solid NaO_2 on the cathode similar to what happens for LiO_2.[35] To gain more insight on the nucleation and growth mechanism of the NaO_2, we measured the concentration of NaO_2 as a function of time in the electrolyte during the discharge process of the Na–O_2 battery cell using titration experiments (Figure S31 in Section S16, Supporting information). The results shown in Figure S31, Supporting information indicate that initially the concentration of NaO_2 in the electrolyte increased from 10 mM at 1 h to its maximum value of ≈50 mM at 6 h; and then, it decreased down to ≈30 mM after 15 h. This was consistent with Welland et al's model proposed for nucleation and growth of LiO_2 from an electrolyte,[35] where there were three different stages of growth similar to what we found for our Na–O_2 system. As shown in Figure S31, Supporting information, at first, the concentration of NaO_2 in the electrolyte increased sharply from 1 to 6 h in the discharging process passing its solubility limit until it eventually reached the supersaturation limit. Then after reaching this point, NaO_2 particles started growing on the cathode surface, and the concentration of the NaO_2 in the electrolyte started to decrease. Finally, particles continued to grow, and the concentration of NaO_2 in the electrolyte decreased to a constant value of ≈30 mM, that was related to equal formation of new NaO_2 in the electrolyte solution and the NaO_2 deposition on the cathode surface. In this last step, the cubic particles grew on the cathode surface. Therefore, based on changes of the NaO_2 concentration as a function of time in the electrolyte, we could confirm a solution phase nucleation and growth mechanism in our Na–O_2 cell.

In addition, the Na^+ and O_2^- likely formed contact ion pairs based on DFT calculations (Table S3 in Section S7.3, Supporting Information), consistent with a solution phase nucleation and growth mechanism. In addition, it has been reported that the disproportionation of NaO_2 in solution phase is not favorable based on DFT calculations reported by Zhao et al.[36] We have also carried out additional higher-level calculations on disproportionation of a NaO_2 dimer that supports this (Table S3, Supporting Information). The formation of NaO_2 in a dry electrolyte is consistent with an experiment we performed in which a small amount of water (1200 ppm) was added to the electrolyte and resulted in the formation of solid Na_2O_2 and NaOH instead of NaO_2 (Section S17, Supporting Information).[37]

The reason for the long cycle life of over 1000 cycles for this NaO_2 based battery is threefold, all related to reducing the reactivity of interfaces involved (**Figure 7**). First, the VP nanoparticles combined with the EMIM-BF_4/TEGDME electrolyte is an effective catalyst system. Evidence for this is that the addition of the EMIM-BF_4 ionic liquid to the TEGDME electrolyte results in a higher activity of VP cathode catalyst than TEGDME by itself (Section S5.3, Supporting Information) and reduces the polarization gap (0.08 V with ionic liquid vs 0.69 V without ionic liquid after 10 cycles; Figure S24 in Section S11, Supporting Information). This is probably because the ionic liquid limits O_2 dissociation on the VP surface according to the DFT results discussed above, which enables the VP to be a more effective electrocatalyst for oxygen reduction.

Second, the ionic liquid may also have a role in preventing parasitic reactions on the NaO_2 surface from the TEGDME where such parasitic reactions were observed in the case of a NaO_2 based battery using a monoglyme electrolyte.[33] This could be another reason for the improved cycle life of the Na–O_2 battery. The evidence for the lack of these parasitic reactions on the NaO_2 surface with the ionic liquid added to the electrolyte is that no CO_2 is present in DEMS during charge (Figure 5f), and there is no carbonate present in the Raman spectra (Figure 5b). We have carried out ab initio molecular dynamics studies that indicate the ionic liquid will be near the surface of NaO_2 (Figure S20 in Section S7.4, Supporting Information), so that it may have a role in preventing any parasitic TEGDME reactions with the NaO_2 surface that could give carbonate products.

The third reason for the long cycle life in the reported Na–O_2 battery is the use of the NaBr protective coating on Na anode. It enables more cycles than NaCl (260 cycles) and NaI (650 cycles)

as protection coatings (Figure S11 in Section S5.6, Supporting Information). An effective protective coating such as NaBr prevents side reactions between oxygen or superoxide anions with the Na anode, as well as providing for good Na^+ transport at the anode/electrolyte interface.

The Na–O_2 cell with a VP cathode and a NaBr protective coating is run for one deep discharge and charge cycle at a current density of 0.1 mA cm^{-2} up to a capacity of 6.5 mAh cm^{-2} (Section S18, Supporting information). Figure S34, Supporting information indicates that the Na–O_2 cell is able to discharge and charge with potentials of 2.15 and 2.40 V, respectively. This deep discharge capacity suggests that with further development, this Na–O_2 battery has the potential to reach a high gravimetric energy density of ≈400 Wh kg^{-1}, which is ≈two times larger than that of the current Na-ion batteries (Section S18, Supporting Information).

3. Conclusion

These results demonstrate evidence that it is possible to have a reversible one-electron discharge process that forms only NaO_2 in a Na–O_2 battery cell with long cycle life using a proper catalyst–electrolyte–anode design that reduces interfacial reactivity. The combination of a highly active VP catalyst, effective Na anode protection by the NaBr coating, and ionic liquid added to the TEGDME electrolyte enables this battery cell to be rechargeable for many cycles with a low polarization gap at a reasonably high rate, which is in contrast with previous studies where only limited cycle life was achieved because of formation of non-desired sodium species during the discharge process. This new Na–O_2 battery cell architecture offers a new pathway for the practical realization of this technology.

4. Experimental Section

Synthesis of TMP Nanoparticles and Cathode Electrode: The transition metal phosphide nanoparticles, vanadium phosphide (VP), molybdenum phosphide (MoP), tri-molybdenum phosphide (Mo_3P), di-iron phosphide (Fe_2P), tri-iron phosphide (Fe_3P), and di-nickel phosphide (Ni_2P) were synthesized by a chemical vapor transport (CVT), at the specific stoichiometry ratios of the corresponding pure elements; that is, Vanadium (99.9%, Sigma–Aldrich), Nickle (99.7%, Sigma–Aldrich), Iron (99%, Sigma–Aldrich), Molybdenum(99.9%, Sigma–Aldrich), and Phosphorus, red (99.99%, Sigma–Aldrich) were mixed in a total loading weight of 1 g and vacuum sealed in a quartz ampule. The quartz ampule was heated in two zone tubular furnace to 1080 °C within 24 h, and then, the hot zone was kept at 1080 °C for 4 days and the cold zone was lowered to 900 °C over 4 days to form pure crystals with pristine structure. For preparation of cathode electrode, synthesized TMP nanoparticles were mixed with Vulcan XC-72R (9:1 w/w) in 20 mL of 2-propanol (Sigma–Aldrich, ACS grade) by an ultrasonic liquid processor (Sonics, Vibra-Cell VCX 130 with a 3.00 mm probe) The final solution was then centrifuged and the top two-thirds of the centrifuged sample, the supernatant, was stored as the catalyst ink. A 1 cm^2 gas diffusion layer (GDL Sigracet 39 BB, thickness = 315 µm, specific area ≈ 95 g m^{-2}, FuelCellStore) was used as the air breathing cathode substrate, which was air-brushed (Speedaire, nozzle size = 0.013 in) with the catalyst ink. The amount of catalyst loading was controlled at 0.1 mg cm^{-2}.

Preparation of the Electrolyte: The liquid electrolyte was first prepared by dissolving 1 M sodium trifluoromethanesulfonimide (NaTFSI, 97% trace metal basis, Sigma–Aldrich) dissolved in a mixture of tetraglyme (Reagent Plus, 99%, Sigma–Aldrich):EMIM-BF_4 (for electrochemistry, ≥ 99.0%, Sigma–Aldrich) with 3:1% v/v, and then, 25 mM each of 2,2,6,6-tetramethyl-1-piperidinyloxyl (TEMPO) (99%, Sigma–Aldrich) and 2,5-di-tert-butyl-1,4-benzoquinone (DBBQ) (98%, Sigma–Aldrich) as redox mediators (RMs) were added to it.

Preparation of Na Anode Protection Coatings: Sodium anode protection coatings were synthesized by reacting chloropropane (for synthesis, Sigma–Aldrich), iodopropane (for synthesis, Sigma–Aldrich), and bromopropane(for synthesis, Sigma–Aldrich) with metallic Na ingot (99.95% trace metal basis, Sigma–Aldrich) under vacuum conditions. Initially, the Na ingot was cut into smaller pieces using a sharp knife inside an argon-filled glovebox. The surfaces of the Na pieces were then scratched to obtain shiny metallic Na. Cleaned Na pieces were pressed on a stainless-steel disc to achieve a certain thickness. The Na anodes were cut into small discs using a puncher, and their surfaces were again scratched to obtain shiny Na anodes. The final thickness of the Na anodes was ≈0.3 mm. The prepared Na anodes were placed in a custom-made holder, and bromopropane, chloropropane, and iodopropane were added for coating. The sodium anodes were then transferred into the glovebox chamber and vacuumed for 5 min, resulting in the formation of sodium halide coating; while, hexane evaporated due to its low boiling point. The sodium anodes with halide protection coatings were stored in an Ar environment for further use.

X-Ray Diffraction (XRD) Spectroscopy: XRD experiments for the TMP nanoparticles and Na protection coatings were carried out using a RIGAKU ATX-G workstation that used a nickel (Ni)-filtered copper (Cu) Kα anode, a multilayer optic monochromator, and a high-count-rate scintillation detector over the range $10° < 2\theta < 100°$ with a step size of 0.02° and a counting time of 1 s $step^{-1}$. All other parameters were chosen to enhance the signal to noise in the spectra. The coated Na anodes were all sealed in a custom-made sample holder with Kapton tape on top to avoid any contamination.

X-Ray Photoelectron Spectroscopy (XPS) Spectroscopy: XPS experiments were performed to obtain the chemical composition of VP nanoparticles and protected Na anodes. Samples were stored in a sealed vial under Ar environment and transferred into the XPS chamber using a mobile glovebox to avoid any contamination. XPS experiments were performed using a Thermo-Scientific ESCALAB 250Xi instrument equipped with an electron flood and scanning ion gun. All the XPS measurements, including peak normalizations and binding energies, were based on the C 1s C—C bond at 284.8 eV. A Shirley background was used to consider the inelastic scattering for the curve-fitting using Thermo-Avantage software.

Scanning Transmission Electron Microscopy (STEM): High-resolution scanning transmission electron microscopy (HR-STEM) experiments were conducted on VP nanoparticles at the atomic scale using a spherical aberration corrected JEOL JEM-ARM 200CF STEM with a cold field emission gun operating at 200 kV, with 22 mrad convergence angle. To achieve this, VP nanoparticles were dispersed in methanol and deposited onto a copper grid using the drop-casting method. The high-angle annular dark-field (HAADF) and annular bright field (ABF) images were taken using an Orius CCD camera with 512 × 512 scanning resolution.

Scanning Electron Microscopy (SEM): SEM imaging was performed using JEOL scanning electron microscope JSM-IT800HL. For SEM experiments, a similar Na–O_2 battery cell was assembled and discharged at a current density of 0.1 mA cm^{-2}. The discharged cathode was extracted in an Ar-filled glovebox with O_2 and humidity level below 1 ppm, and then, rinsed with anhydrous DMC to remove electrolyte residues. The sample was then transferred to a sealed vial, and then, rapidly handled for the SEM imaging to avoid any possible transformation within the formed species during the discharge process. Images were obtained in secondary electron mode using an accelerating voltage of 15–3 keV.

Focused Ion Beam/SEM: The anode morphology was characterized using a Thermo Fischer Scientific Helios 5 CX focused-ion beam (FIB)/SEM DualBeam system at the University of Illinois Chicago. The Na anode samples with protective halide coating were transferred from the glovebox to a vacuum cryo transfer system (Leica EM VCT500) in an Ar-filled container. The sample container was plunged into a liquid N_2 bath and subsequently cooled to liquid N_2 temperature. The cooled container was opened under a high liquid N_2 level such that the anode surface was completely

submerged under the liquid N_2 level, minimizing any air exposure. The sample was then transferred to the cryo-FIB/SEM using a transfer shuttle. The temperature of the transfer shuttle was maintained at −150 °C during sample transfer. The sample temperature was maintained at −193 °C inside the cryo-FIB/SEM during the experiments.

Raman Spectroscopy Experiments: Raman spectra were collected using a Horiba LabRAM HR Evo Confocal Raman. A 532 nm laser source, 600 g mm^{-1} grating, and a custom-designed LCD objective with an adjustable aberration correction were organized to probe the glass-sealed samples. The measurement parameters such as acquisition time, averaging parameters, and laser power were all optimized to enhance the signal-to-noise ratio of the spectra. Raman spectroscopy experiments were carried out for the discharge and charge processes of different cycles.

In Situ Differential Electrochemical Mass Spectroscopy (DEMS): A Hiden HPR-40 DEMS membrane inlet mass spectrometer (MIMS) was utilized to accurately measure the e^-/O_2 transferred during the charge process of the Na–O_2 battery cell under investigation. To calibrate the O_2 signal of the DEMS instrument, a custom-made sample loop with known volumes (0.02, 0.05, 0.1, and 0.25 mL) was used. The moles of O_2 in each sample were calculated based on standard temperature and pressure conditions (1 mole of gas having a volume of 22.4 L at 1 atm pressure). In situ DEMS experiments were executed using a custom-designed Swagelok battery cell (EQ-STC-LI-AIR, MTIXTL) after discharging it at a current density of 0.1 mA cm^{-2}. The battery cell was then connected to the DEMS instrument and flushed with Ar (UHP, Airgas) for 15 min to eliminate gas impurities; while, the DEMS instrument was in operation. The connection to the DEMS instrument was maintained until the O_2 signal reached a steady state, which took approximately an hour. Next, the Na–O_2 battery cell was charged at a current density of 2 A g^{-1} (0.2 mA cm^{-2}) for 30 min, resulting in a capacity of 1 Ah g−1. Throughout the charge process, the DEMS signals for O_2, H_2O, and CO_2 were continuously monitored (Figure 5f in the manuscript).

Preparation of Na–O_2 Cell Battery: All cells were assembled in an Ar-filled glovebox with O_2 and humidity levels below 1 ppm. Identical custom-made Na–O_2 battery cells with two needle valves and a pressure gauge, to house 40 µL of an electrolyte soaked in a Whatman GF/A Glass Microfiber filter (Sigma-Aldrich), were used as the separator/electrolyte with Na anodes and the TMP based cathodes. The battery cells were then transferred out of the glovebox with valves remaining closed to avoid any contamination. The battery cells were flushed with Ar (UHP, Airgas) to remove any possible trace impurity, and then, filled with O_2 (UHP, Airgas) to a relative pressure of 0.12 MPa.

Electrochemical Measurements: To determine the ionic conductivity of the electrolyte, an electrochemical impedance spectroscopy (EIS) experiment, employing an AC impedance spectrum, was conducted. The experiment utilized a symmetric SS|Electrolyte|SS electrochemical cell. The AC impedance measurements were performed at room temperature, covering a frequency range from 100 kHz to 0.1 Hz and applying an AC signal of 5 mV. This signal strength was chosen as it generated a suitable signal-to-noise ratio; while, inducing a strongly linear current. The EIS experiment was carried out using a BioLogic potentiostat SP150. Cyclic voltammetry (CV) experiments were performed to measure the oxygen evolution and reduction (OER and ORR, respectively) using TMP-based nanoparticles as catalysts. A custom-designed electrochemical cell was employed by using a pristine Na metal disc serving as the counter electrode and the reference electrode and the TMP-based cathode as the working electrode. Cyclic voltammetry (CV) experiments were performed by sweeping the potential between 1.5 and 4.5 V versus Na/Na^+ at a scan rate of 0.5 mV s^{-1} using BioLogic potentiostat SP150.

DFT Simulation: Vienna ab initio simulation package (VASP) was employed for periodic density functional theory (DFT) calculations. The GGA-PBE functional was used to determine electron–electron exchange-correlation energies, and the projector-augmented wave (PAW) method was employed for core-valence interactions. Kohn–Sham wave functions were expanded using a plane-wave basis set, and the Monkhorst–Pack grid was utilized for reciprocal Brillouin zone integrations. The bulk structures of Na, NaCl, NaBr, NaI, and VP were optimized with a cut-off energy of 600 eV and a 10 × 10 × 1 k-point mesh. For the slab models of Na and VP, a cut-off energy of 400 eV was applied. Ionic relaxation was performed iteratively until the force on each atom was below 0.02 eV $Å^{-1}$. Due to allowing relaxation on only one side of the slab model, dipole corrections were incorporated into all calculations.

Supporting Information

Supporting Information is available from the Wiley Online Library or from the author.

Acknowledgements

M.A. acknowledges support from the U.S. Department of Energy under Contract DE-AC02-06CH11357 from the Vehicle Technologies Office, Office of Energy Efficiency and Renewable Energy. The authors also acknowledge supports from the Wanger Institute for Sustainable Energy Research (WISER) and IIT's Armour College of Engineering. The authors acknowledge the Keck-II facility of Northwestern University's NUANCE Center, which has received support from the SHyNE Resource (NSF ECCS-1542205); the MRSEC program (NSF DMR-1720139) at the Materials Research Center; the International Institute for Nanotechnology (IIN); the Keck Foundation; and the State of Illinois, through the IIN. The work at Argonne was supported by the U.S. Department of Energy under Contract DE-AC02-06CH11357 from the Vehicle Technologies Office, Office of Energy Efficiency and Renewable Energy. This work made use of the Thermo Fisher Helios 5CX (cryo)FIB-SEM instrument in the Electron Microscopy Core of UIC's Research Resources Center, which received support from UIC, Northwestern University and ARO (W911NF2110052). A.S.T. and R.F.K. were supported by grants from the National Science Foundation (NSF-CBET 2312359) and Army Research Office under Grant Number W911NF-23-1-0225. R.S.-Y. acknowledges the financial support from NSF DMR-1809439. The views and conclusions contained in this document are those of the authors and should not be interpreted as representing the official policies, either expressed or implied, of the Army Research Office or the U.S. Government. The U.S. Government is authorized to reproduce and distribute reprints for Government purposes notwithstanding any copyright notation herein. The submitted manuscript has been created by UChicago Argonne, LLC, Operator of Argonne National Laboratory ("Argonne"). Argonne, a U.S. Department of Energy Office of Science laboratory, is operated under Contract No. DE-AC02-06CH11357. The U.S. Government retains for itself, and others acting on its behalf, a paid-up nonexclusive, irrevocable worldwide license in said article to reproduce, prepare derivative works, distribute copies to the public, and perform publicly and display publicly, by or on behalf of the Government. The Department of Energy will provide public access to these results of federally sponsored research in accordance with the DOE Public Access Plan. http://energy.gov/downloads/doe-public-access-plan.

Conflict of Interest

The authors declare no conflict of interest.

Author Contributions

A.A. and A.K. synthesized the TMP nanoparticles and the halide-based anode protection layers. A.A., A.K., M.G.P., A.M.H., G.-Y.K., and P.N.M.D. carried out SEM, XRD, XPS, Raman spectroscopy, DEMS, and battery experiments. M.A. supervised the experimental efforts in design, synthesis, characterization, and electrochemical testing and analyses. M.T.S. and R.S.-Y. performed STEM analyses of the cathode. A.S.T. carried out the cryo-FIB/SEM experiments under the supervision of R.F.K. N.S. and A.T.N. performed DFT calculations. L.A.C. helped with deducing the reaction mechanism based on the experimental observations and DFT calculations. All authors contributed to the manuscript before submission.

Data Availability Statement

The data that support the findings of this study are available from the corresponding author upon reasonable request.

Keywords

ionic liquid, metal–air battery, Sodium Bromide protection coating, sodium–oxygen battery, vanadium phosphide (VP) nanoparticles

Received: October 10, 2024
Revised: December 20, 2024
Published online: February 4, 2025

[1] B. L. Ellis, L. F. Nazar, *Curr. Opin. Solid State Mater. Sci* **2012**, *16*, 168.
[2] S. K. Das, S. Lau, L. A. Archer, *J. Mater. Chem. A* **2014**, *2*, 12623.
[3] K. Song, D. A. Agyeman, M. Park, J. Yang, Y. M. Kang, *Adv. Mater.* **2017**, *29*, 1606572.
[4] B. D. McCloskey, J. M. Garcia, A. C. Luntz, *J. Phys. Chem. Lett.* **2014**, *5*, 1230.
[5] P. Hartmann, C. L. Bender, M. Vračar, A. K. Dürr, A. Garsuch, J. Janek, P. Adelhelm, *Nat. Mater.* **2012**, *12*, 228.
[6] H. Yadegari, X. Sun, *Trends Chem.* **2020**, *2*, 241.
[7] C. L. Bender, D. Schröder, R. Pinedo, P. Adelhelm, J. Janek, *Angew. Chem., Int. Ed.* **2016**, *55*, 4640.
[8] X. Bi, R. Wang, L. Ma, D. Zhang, K. Amine, J. Lu, *Small Methods* **2017**, *1*, 1700102.
[9] X. Bi, R. Wang, K. Amine, J. Lu, *Small Methods* **2019**, *3*, 1800247.
[10] H. Yadegari, Y. Li, M. N. Banis, X. Li, B. Wang, Q. Sun, R. Li, T. K. Sham, X. Cui, X. Sun, *Energy Environ. Sci.* **2014**, *7*, 3747.
[11] A. Von Gunten, K. Velinkar, E. Nikolla, J. Greeley, *Chem. Mater.* **2023**, *35*, 5945.
[12] L. Lutz, W. Yin, A. Grimaud, D. Alves Dalla Corte, M. Tang, L. Johnson, E. Azaceta, V. Sarou-Kanian, A. J. Naylor, S. Hamad, J. A. Anta, E. Salager, R. Tena-Zaera, P. G. Bruce, J.-M. Tarascon, *J. Phys. Chem. C* **2016**, *120*, 20068.
[13] J. Kim, H. Park, B. Lee, W. M. Seong, H.-D. Lim, Y. Bae, H. Kim, W. K. Kim, K. H. Ryu, K. Kang, *Nat. Commun.* **2016**, *7*, 10670.
[14] K. K. Velinkar, A. Von Gunten, J. Greeley, E. Nikolla, *ACS Energy Lett.* **2023**, *8*, 4555.
[15] C. L. Bender, P. Hartmann, M. Vračar, P. Adelhelm, J. Janek, *Adv. Energy Mater.* **2014**, *4*, 1301863.
[16] W. Liu, Q. Sun, Y. Yang, J.-Y. Xie, Z.-W. Fu, *Chem. Commun.* **2013**, *49*, 1951.
[17] C. Xia, R. Black, R. Fernandes, B. Adams, L. F. Nazar, *Nat. Chem.* **2015**, *7*, 496.
[18] N. Ortiz-Vitoriano, T. P. Batcho, D. G. Kwabi, B. Han, N. Pour, K. P. C. Yao, C. v. Thompson, Y. Shao-Horn, *J. Phys. Chem. Lett.* **2015**, *6*, 2636.
[19] P. Hartmann, C. L. Bender, J. Sann, A. K. Dürr, M. Jansen, J. Janek, P. Adelhelm, *Phys. Chem. Chem. Phys.* **2013**, *15*, 11661.
[20] P. Hartmann, D. Grübl, H. Sommer, J. Janek, W. G. Bessler, P. Adelhelm, *J. Phys. Chem. C* **2014**, *118*, 1461.
[21] T. Liu, G. Kim, M. T. L. Casford, C. P. Grey, *J. Phys. Chem. Lett.* **2016**, *7*, 4841.
[22] Q. Sun, L. Dai, T. Luo, L. Wang, F. Liang, S. Liu, *Carbon Energy* **2023**, *5*, e276.
[23] Z. Zheng, J. Jiang, H. Guo, C. Li, K. Konstantinov, Q. Gu, J. Wang, *Nano Energy* **2021**, *81*, 105529.
[24] N. Zhao, C. Li, X. Guo, *Phys. Chem. Chem. Phys.* **2014**, *16*, 15646.
[25] L. Ma, D. Zhang, Y. Lei, Y. Yuan, T. Wu, J. Lu, K. Amine, *ACS Energy Lett.* **2018**, *3*, 276.
[26] H. Yadegari, Q. Sun, X. Sun, *Adv. Mater.* **2016**, *28*, 7065.
[27] H. Yadegari, M. Norouzi Banis, A. Lushington, Q. Sun, R. Li, T.-K. Sham, X. Sun, *Energy Environ. Sci.* **2017**, *10*, 286.
[28] B. Wang, N. Zhao, Y. Wang, W. Zhang, W. Lu, X. Guo, J. Liu, *Phys. Chem. Chem. Phys.* **2017**, *19*, 2940.
[29] J. T. Frith, I. Landa-Medrano, I. Ruiz de Larramendi, T. Rojo, J. R. Owen, N. Garcia-Araez, *Chem. Commun.* **2017**, *53*, 12008.
[30] B. Sun, K. Kretschmer, X. Xie, P. Munroe, Z. Peng, G. Wang, *Adv. Mater.* **2017**, *29*, 1606816.
[31] C. Sheng, F. Yu, Y. Wu, Z. Peng, Y. Chen, *Angew. Chem.* **2018**, *130*, 10054.
[32] P. Hartmann, M. Heinemann, C. L. Bender, K. Graf, R.-P. Baumann, P. Adelhelm, C. Heiliger, J. Janek, *J. Phys. Chem. C* **2015**, *119*, 22778.
[33] L. Lutz, W. Dachraoui, A. Demortière, L. R. Johnson, P. G. Bruce, A. Grimaud, J. M. Tarascon, *Nano Lett.* **2018**, *18*, 1280.
[34] C. Sheng, F. engjiao Yu, Y. uping Wu, Z. Peng, Y. Chen, *Angew. Chem.* **2018**, *130*, 10054.
[35] M. J. Welland, K. C. Lau, P. C. Redfern, L. Liang, D. Zhai, D. Wolf, L. A. Curtiss, *J. Chem. Phys.* **2015**, *143*, 224113.
[36] S. Zhao, C. Wang, D. Du, L. Li, S. Chou, F. Li, J. Chen, *Angew. Chem.* **2021**, *133*, 3242.
[37] R. Pinedo, D. A. Weber, B. Bergner, D. Schröder, P. Adelhelm, J. Janek, *J. Phys. Chem. C* **2016**, *120*, 8472.